ELSEVIER

Nuclear Instruments and Methods in Physics Research A 452 (2000) 192–204

NUCLEAR INSTRUMENTS & METHODS IN PHYSICS RESEARCH Section A

www.elsevier.nl/locate/nima

Laboratory tests on neutron shields for gamma-ray detectors in space

J. Hong*, W.W. Craig, C.J. Hailey

Columbia Astrophysics Laboratory, Columbia University, 538 W. 120th Street, New York, NY 10027, USA

Received 19 January 2000; accepted 17 March 2000

Abstract

Shields capable of suppressing neutron-induced background in new classes of γ-ray detectors such as CdZnTe are becoming important for a variety of reasons. These include a high cross section for neutron interactions in new classes of detector materials as well as the inefficient vetoing of neutron-induced background in conventional active shields. We have previously demonstrated through Monte-Carlo simulations how our new approach, supershields, is superior to the monolithic, bi-atomic neutron shields which have been developed in the past. We report here on the first prototype models for supershields based on boron and hydrogen. We verify the performance of these supershields through laboratory experiments. These experimental results, as well as measurements of conventional monolithic neutron shields, are shown to be consistent with Monte-Carlo simulations. We discuss the implications of this experiment for designs of supershields in general and their application to future hard X-ray/γ-ray experiments.

Keywords: Neutrons; Background; Supershields

1. Introduction

Balloon-borne or satellite-based γ-ray telescopes intended for astrophysical observations typically have count rates that are dominated by background. Sensitivity improvement is typically achieved by increasing the area of the detector and by introducing active shields to veto external background. As conventional active shield technology has improved, the neutron-induced background has become increasingly important.

Neutron-induced background, which has both prompt and delayed components, is due to both atmospheric albedo neutrons as well as neutrons generated by secondary interactions in the material surrounding the detector (i.e. the spacecraft, instrument support structure and the detector shielding). Conventional active shields are inefficient at vetoing the neutron-induced background [1]. Increasing the size of the shields is not generally helpful because the increased mass raises the secondary particle production. Neutron-induced background can be the dominant component of the total background in new classes of detectors, such as CdZnTe sensors shielded with an active material such as BGO or traditional alkali halides [1,2].

The Ge spectrometer with BGO shields on INTEGRAL is an example of a conventional configuration [3]. The BGO and plastic shields are

* Corresponding author.
E-mail address: flame@zen.phys.columbia.edu (J. Hong).

0168-9002/00/$ - see front matter
PII: S0168-9002(00)00428-9

optimally configured for efficient rejection of γ-ray and charged particle background. Further sensitivity improvement is limited by intrinsic background, such as secondary particle production in the shields [4].

Neutron-induced background, in particular, the activation of material by the incoming neutron flux, can produce numerous hard X-ray/γ-ray decay lines as well as a photon continuum ranging from 10 keV to 10 MeV. Many important astrophysical sources are also expected to produce decay lines from radioactive sources, such as ^{26}Al from the galactic plane or ^{56}Co, ^{56}Ni and ^{44}Ti from supernovae [5]. Photon contamination caused by the neutron-induced background must be removed to make full use of the high resolution in future high-sensitivity hard X-ray/γ-ray missions.

We introduced the supershield concept to address the neutron-induced background problem [1]. Supershields are designed to shield both the neutron-induced background and other external background sources. The standard supershield configuration consists of three separate layers; a conventional active shield, a neutron moderator, and a neutron absorber.

Neutron shields for γ-ray detectors were investigated a decade ago [6,7]. We have previously reported on our Monte-Carlo simulations that demonstrated the improved performance of the supershield concept as compared to conventional neutron shields [8]. The separate layers of neutron absorber and moderator material in the supershield configuration not only increase the neutron shielding efficiency but also suppress low-energy neutrons generated in the shield, one of the major problems in previous attempts to develop neutron shields.

In this paper we describe the performance of both conventional and prototype supershields using boron and hydrogen. We verify the performance of these shields through laboratory experiments, using mono-energetic neutron beams at the Radiological Research Accelerator Facility (RARAF[1]). The laboratory results are shown to validate the Monte-Carlo simulation results and the supershield concept. In this work we focus primarily on neutron transport through the shields.

2. Experimental setup

2.1. Neutron source

To understand neutron transport through shields, we have to identify the intensity and spectrum of incoming and outgoing neutrons. We use an RARAF beam to irradiate the shields with mono-energetic neutrons. A ^{3}He gas proportional counter is used to measure both high- and low-energy neutrons. Several boron- and hydrogen-based shields were constructed and tested. The overall setup of the experiment is illustrated in Fig. 1.

2.2. Neutron source

RARAF provides a source of mono-energetic neutrons designed for studies in radiation biology, dosimetry, and micro-dosimetry. The primary hydrogen and deuterium beams generated by a Van der Graaff accelerator are used to produce secondary beams of neutrons by nuclear reactions in thin targets. Neutron spectroscopy often uses a time-of-flight measurement technique in order to get precise neutron energy spectra. RARAF is not equipped to perform time-of-flight measurements but does produce mono-energetic neutron beams that simplify the calibration procedures for neutron detectors. Neutrons in the energy range from 100 keV to 14 MeV can be readily produced.

For these experiments we used a Ti-coated tritium target (Ti thickness = 2.224 mg/cm^2, tritium/Ti ratio = 2.10) to produce neutrons from 500 keV to 3 MeV. The neutrons in this energy range are most relevant as the evaporative secondary neutrons produced in material surrounding a hard X-ray/γ-ray instrument usually have a few MeV energy [8].

Neutrons at lower energies ($\lesssim$100 keV), i.e. atmospheric neutrons, are not as much of a problem because of higher neutron absorption cross sections of shielding materials at lower energies. Neutrons

[1] Radiological Research Accelerator Facility at Nevis Laboratories, Columbia University, P.O. Box 21, Irvington, NY 10533, USA.

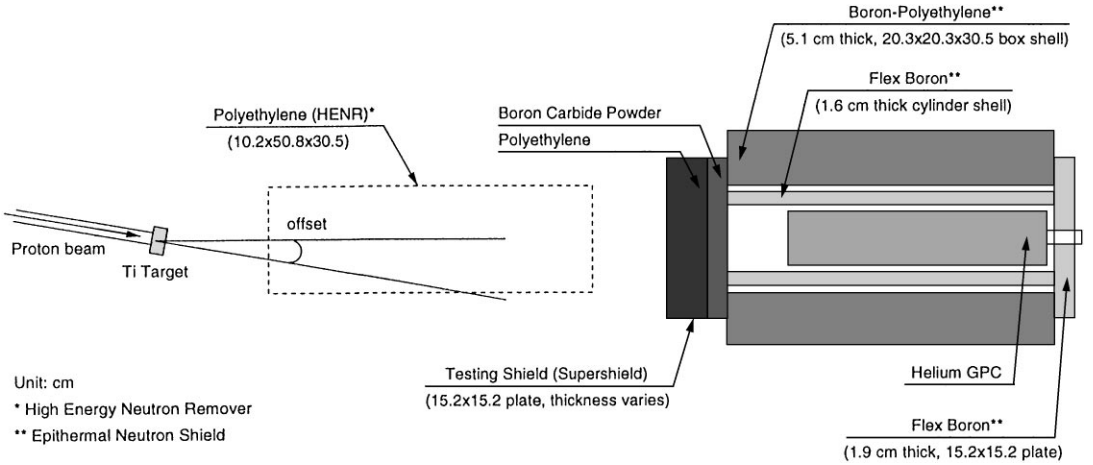

Fig. 1. A cross-sectional view of the experimental setup at RARAF: A shield configuration using boron carbide powder with polyethlene is being tested. A flexible boron material and boron-polyethylene around the detector are used to reduce the effects from ambient epithermal neutrons. The polyethylene block shown as dotted lines removes high energy neutrons and is referred to as a High Energy Neutron Remover or HENR in the text. For each shield configuration the measurements are conducted with/without the HENR in order to identify the effects of the residual epithermal neutrons.

at higher energies ($\gtrsim 100$ MeV), such as cascade neutrons, can also be neglected as they have a relatively small cross section with the detector material.

Neutrons emerge isotropically from the thin film target and their energies are determined by the kinematics of the primary proton beam and the outgoing neutrons [9]. To minimize energy spread, our experiments are conducted at 100° (the offset in Fig. 1) from the primary beam direction for neutrons in the energy range from 500 keV to 1 MeV, and at an offset of 10° for the neutrons above 1 MeV.

Fig. 2 shows the energy distributions of the neutrons on a 20×20 cm^2 area 51 cm away from the target. We analyzed the results for two neutron source energies as shown in Fig. 2. The average energies are ~ 1 and ~ 2 MeV, respectively. For simplicity we term these "1-MeV" and "2-MeV" neutrons.

In addition to the 1-MeV or 2-MeV neutron source generated directly from the target, there are background neutrons of other energies present during the measurements. All the neutrons produced in the target eventually interact with equipment or the walls of the experimental hutch. The neutrons moderated by these interactions are called epithermal neutrons.[2] When the primary proton beam is on, the room is filled with the epithermal neutrons, which must be distinguished from the low-energy neutrons coming from the test shields (refer to Section 2.4).

2.3. Neutron detectors

Because the cross section for neutron interactions with most materials is a strong function of neutron energy, rather different techniques have been developed for neutron detection in different energy regions [10]. We used a ^{3}He gas proportional counter to detect low- and high-energy neutrons simultaneously. The properties of the detector are listed in Table 1.

Like common proportional counters or scintillators, ^{3}He counters cannot spectroscopically resolve few-eV neutron energies due to the high

[2] The meaning of epithermal neutrons varies in the literature. Here they are defined as neutrons that have been moderated by the environment into the sub-thermal through low-energy region. These moderated neutrons all deposit the same energy (the reaction Q-value) in the detector. The resulting peak in the detector response is called the epithermal peak.

reaction Q-value. The detector simply serves as a counter for low-energy neutrons. We utilized a pulse rise-time discrimination technique (see Fig. 3) to use the ^{3}He counter as a high-energy neutron spectrometer ($\sim$ 500 keV–8 MeV) [11,12].

Compared to crystal or plastic scintillators, gas proportional counters are efficient at detecting neutrons in high γ-ray background environments because of their relatively low stopping powers for γ-rays. Unlike proportional counters used in the soft X-ray passband, the windowless counters we use for neutron detection can have relatively thick walls, which block soft X-rays. Consequently, in the ^{3}He counter the energy region analyzed in this paper ($>$ 500 keV) is free of γ-ray background.

Table 1
The properties of the ^{3}He gas proportional counter used as the primary detector in these experiments (Model 2531 from LND, Inc.)

Parameter	Value
Interaction	^{3}He(n, p)T (Q-value: 764 keV)
Components	CO_2:Ar:^{3}He = 91:1520:2950 (Torr)
Size (cylinder)	5.1×24.8 cm^2 (diameter $\times$ length)
Resolution	$\lesssim$10% at 1 MeV
Efficiency	$\sim$ 100% ($\lesssim$1 eV), $\sim$ 1% (1 MeV)

^{3}He counters are subject to a "wall effect", the result of incomplete pulse collections caused by collisions between the detector wall and the secondary particles of neutron interactions [13]. The response function of the ^{3}He counter is distorted by

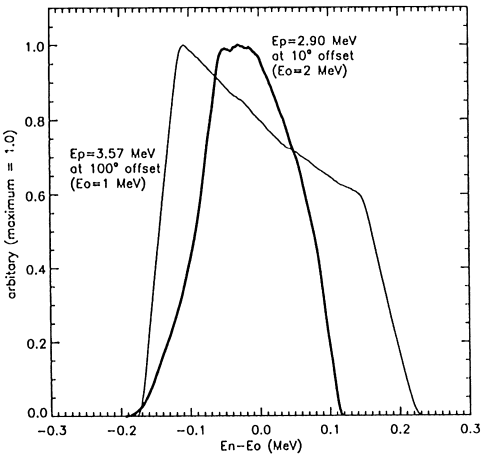

Fig. 2. The energy distributions of neutrons (E_n) generated by T(p, n)^3 He interaction at RARAF. The energy distributions are from neutrons impinging on a 20×20 cm^2 imaginary window 51 cm away from the target. The energies of the primary proton beams (E_p) are 2.90 and 3.57 MeV, and the windows are located at 10 and 100 degrees off the direction of the primary proton beams. The spread in energy is primarily due to the thickness of the target and the size of the window.

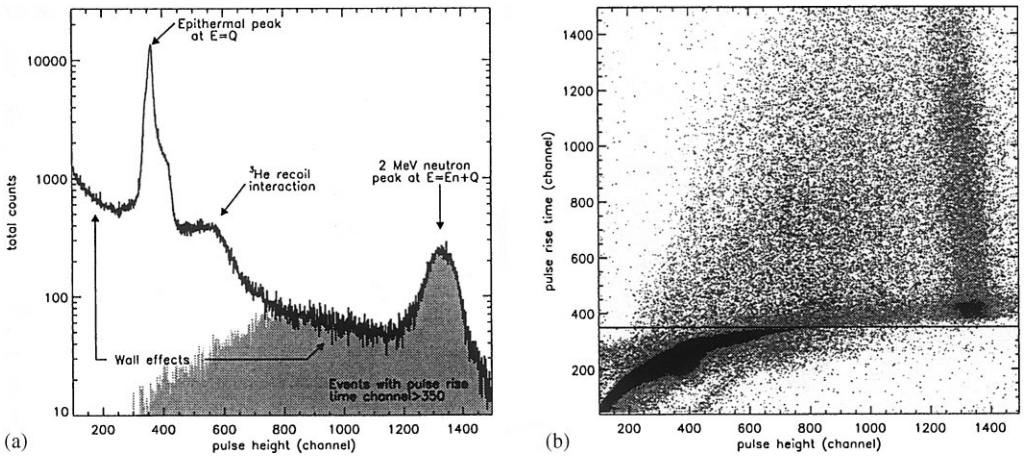

Fig. 3. The response of the ^{3}He counter from 2 MeV neutrons: (a) Pulse height histogram: The 2 MeV neutrons produce a peak at $E_n + Q = 2.764$ MeV and also create a recoil bump, which ends around 1.5 MeV. The shaded region is from the events with pulse rise time slower than $\sim$ 1.4 μs; (b) a two-dimensional map of pulse height and rise time from 2 MeV neutrons on a semi-log gray scale: The recoil events have faster rise times than ^{3}He(n, p)T interactions. Channel 350 on y-axis, shown as a line, is about 1.4 μs in rise time.

the wall effect as well as other competing interactions (e.g. recoil interaction). Pulse rise time can be used quite effectively to separate these various effects. Fig. 3 shows the pulse height histogram of the ^{3}He counter illuminated by a 2 MeV neutron beam and a two-dimensional map of pulse rise times versus pulse heights. Here the pulse rise-time information is used to select high-energy neutron events. The events with a pulse rise time slower than 1.4 μs are from ^{3}He(n,p)T interactions of high-energy neutrons. Events faster than this are due to recoil interactions or from the epithermal neutrons.

The long axis of the cylindrical ^{3}He counter was set to point directly at the Ti target to maximize the neutron path length in the detectors (Fig. 1). The counter was placed $\sim$ 80 cm from the Ti target to minimize energy dispersion at the detection point (the farther from the Ti target, the smaller the dispersion) while reducing epithermal neutrons from the wall (the closer to the Ti target, the smaller the epithermal-neutron-induced background).

A tissue-equivalent ionization chamber monitored the variation of the neutron beam intensity. A delay line amplifier (ORTEC 460) and pulse shape analyzer (ORTEC 552) were used to measure the pulse rise time of each event.

2.4. Shields

The standard configuration of a supershield consists of three separate layers that background radiation must traverse before reaching the detector. The first element is a conventional active shield, followed by a layer of neutron moderator and finally a layer of neutron absorber. By first moderating, and then absorbing, the neutrons, the supershield is able to take full advantage of the higher cross section for neutron absorption at lower neutron energies. Alternate supershield configurations, where the active shield is placed inside of the neutron shield are also possible [1].

Here we are interested primarily in the neutron transport through the shields and therefore only the moderator and absorber portion of the shields are tested. To find out how many incident neutrons are moderated and how many of them are absorbed in the shields, we placed a slab of each shield configuration in the path of neutrons, e.g. the polyethylene/boron shield combination shown in Fig. 1.

Table 2
Shielding materials

Material	Elemental analysis (mg/cm^3)	B:H[a]
Boron–polyethylene	B:H:(C, Si, …) = 357:102:731	1.99:6.07
B_4 powder	B:(C, O, …) = 937:382	5.22:0.00
Polyethylene	H:C = 135:765	0.00:8.03
Flex boron[b]	B:H:(Si, O, …) = 416:45:1179	2.32:2.68

[a]The number density ($\times 10^{22}$ atoms/cm^3): Natural boron is 19.9% ^{10}B.
[b]Flex boron is used only for the epithermal neutron shield around the ^{3}He counter.

Table 3
The test shield configurations

Test configurations	Material and thickness (cm)[a]	B:H[b]
No shield[c]	—	—
Epithermal only	—	—
$Poly_{(thin)}$	3.8	0.00:3.06
$Reverse_{(thin)}$[d]	3.8(Poly) + 2.1(B_4C)	1.10:3.06
$Monolithic_{(thin)}$	5.1(Boron–Poly)	1.01:3.08
$Supershield_{(thin)}$	2.1(B_4C) + 3.8(Poly)	1.10:3.06
$Poly_{(thick)}$	7.6	0.00:6.12
$Reverse_{(thick)}$	7.6(Poly) + 4.2(B_4C)	2.19:6.12
$Monolithic_{(thick)}$	10.2(Boron–Poly)	2.02:6.17
$Supershield_{(thick)}$	4.2(B_4C) + 7.6(Poly)	2.19:6.12

[a]Shield dimension is 15.2 cm × 15.2 cm × thickness.
[b]The column density experienced by normal-incident neutrons ($\times 10^{23}$ atoms/cm^2).
[c]All but a small portion of the epithermal neutron shield was removed from the ^{3}He counter.
[d]Material arranged in opposite order from standard supershield. This is different from the "reverse" supershield referred to in Ref. [1].

The basic shielding materials are listed in Table 2. The shield configurations constructed are listed in Table 3. Because nuclear production cross sections are proportional to $A^{2/3}$, low atomic weight materials are preferred to high-weight ones even though a candidate material, such as cadmium, may have a higher cross section for neutron absorption interaction. Further work will test other aspects of the shields, such as secondary particle

production in the shields. The polyethylene, boron–polyethylene and flex boron are bulk materials. Boron carbide powder, encapsulated in an acrylic plastic case, was used to construct the "boron" shield material.

Ten different configurations (including two with no shielding material in front of the detector) were tested. Each shield configuration was tested at two neutron energies (1 and 2 MeV). In order to investigate the difference of shielding performance as a result of different arrangements of the materials, the number densities of boron and hydrogen atoms in all monolithic and supershield configurations were identical to within 10%.

Since epithermal neutrons saturate the ^{3}He counter, it is difficult to find out how many neutrons are moderated only by the test shields. To reduce the epithermal neutron flux entering the detector, we built an epithermal neutron shield using flex boron and boron–polyethylene. The epithermal neutron shield itself is a modified version of a supershield and covers the detector completely except for the side facing the Ti target. The epithermal neutron shield was used in all but the "No Shield" configurations.

Even with the epithermal neutron shield around the detector, we cannot completely eliminate ambient neutrons. To allow correction for their effects, we repeated measurements for each test shield configuration with a $10.2 \times 50.8 \times 30.5$ cm^3 block of polyethylene – termed a high-energy neutron remover (HENR) – in front of the Ti target. We identify epithermal neutron flux entering the detector by removing all the neutrons arriving at the detector directly from the Ti target through the HENR.

3. Analysis

3.1. Simulations

To properly interpret the data from the experiments, we rely on accurate simulations of the experimental setup. For all analysis presented in the paper we utilized the COG package to simulate neutron transport. COG is a high-resolution code for Monte-Carlo simulation of coupled neutron, gamma, and electron transport that was developed and tested at Lawrence Livermore National Laboratory [14]. COG follows all products of neutron interactions and uses discrete physics data rather than the group-averaged neutron data used by older codes. For the simulation input, the energy and emission angle distributions of the neutron source at the target are calculated according to the cross-section table of T(p,n) ^{3}He interaction and related data [9].

The most important issues to understand are the neutron transport through the test shields and the effects of the ambient epithermal neutrons. Simulation of all geometries tested in these experiments is computationally intensive. To save time in simulation, we divided the neutron source into two parts; one heading toward the test shields directly from the target and the other indirectly. The direct beam simulation shows how many high-energy neutrons would be moderated and absorbed by the test shields. The indirect beam simulation highlights the effects of epithermal neutrons.

To increase statistics in the indirect case with a reasonable simulation run time, first we determine the neutron spectra entering a fictitious box housing the epithermal and test shields. In doing so, we include the important elements of the room, such as the detailed target structure, aluminum table and supports, and concrete walls, but exclude the contents of the box. Then, at the surface of the fictitious box, we generate neutrons according to the spectrum resulting from the previous simulation and transport these neutrons through the geometry of the shields and detectors inside the box.

The first step in the indirect beam simulation showed that the epithermal neutron spectrum entering the fictitious box is the same regardless of the presence of the HENR (the polyethylene block in front of the experimental apparatus as shown in Fig. 1). Only the very high-energy parts of the spectra show differences, which are negligible compared to the number of the high-energy neutrons in the direct simulation. This result allows us to treat the epithermal neutron flux with and without the HENR in the same fashion.

Since COG is not designed to handle details of the response of a gas proportional counter (e.g. wall effects) we wrote several routines to take into

account wall effects and to calculate the neutron detection efficiency [13].

3.2. Data analysis

The response function of the ^{3}He counter (Fig. 3a) complicates determination of the precise neutron spectrum entering the detector. In order to find out how many incident neutrons are absorbed and moderated by each shield configuration, it is sufficient to count the numbers of detected high- and low-energy neutrons with the test shields in place and then to compare the counts with those of the "Epithermal Only" shield configuration. All count rates are renormalized to compensate for changes in the neutron beam intensity during the measurements.

The rates in the ^{3}He counter in Fig. 5 are dominated by epithermal neutron flux since the absorption cross section for neutron interactions with ^{3}He is roughly proportional to the inverse of the neutron velocities. This can be verified by noting that the HENR does not make any difference in the "No Shield" configuration (Fig. 4) because the number of high-energy neutrons detected in the ^{3}He counter is very small compared to the measured epithermal neutrons (Fig. 3). This means that most

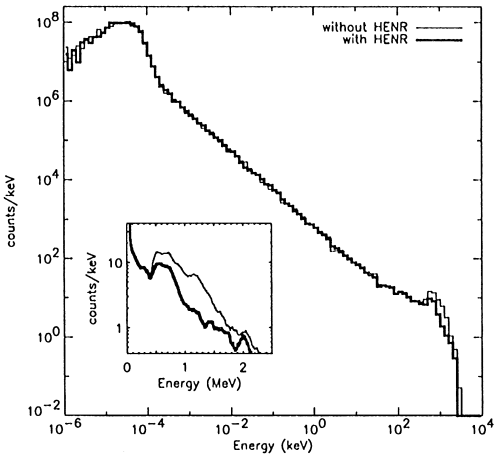

Fig. 4. Epithermal neutron flux entering the fictitious box with a 1 MeV neutron source: Except for the high-energy part of the spectra, there is no difference with/without the polyethylene block (the HENR) that removes the high-energy neutron component.

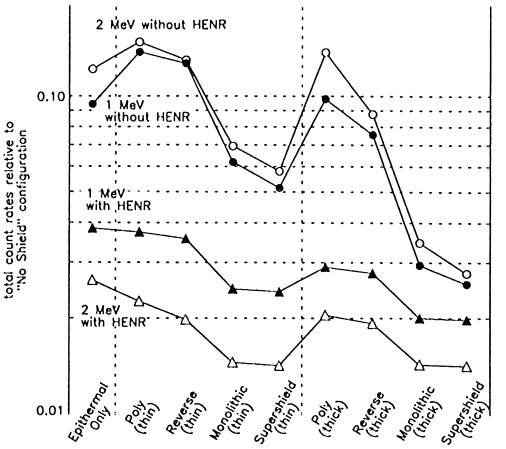

Fig. 5. The total count rate for each test shield configuration relative to "No Shield" configuration: The relative count rates have been normalized as described in the text and clearly demonstrate the effectiveness of the "Supershield" configuration.

of the low-energy neutrons detected are actually epithermal neutrons that must be subtracted out to determine the neutrons moderated by the test shields. Thus, to normalize our count rates we first correct for any (long time-scale) beam fluctuations and then divide by the count rates measured in the "No Shield" configuration. The resultant rates as shown in Fig. 5 demonstrate that, as expected, the epithermal neutron shield reduced the count rate by more than a factor of 10. This procedure allows a clear demonstration of the relative effects of the various shield configurations. Proper arrangements of moderator and absorber increase the efficiency for absorbing neutrons, which is clear from comparing the results of the "Supershield" and "Reverse" configurations, particularly with the high-energy neutrons included. The "Supershield" configuration has the lowest total count rates among the test shield configurations.

3.2.1. Moderation of high-energy neutrons

The high-energy part of the ^{3}He counter response is relatively free of contamination from unwanted neutrons, such as epithermal neutrons and recoil interactions. The counts around the peak at $1 + Q$ or $2 + Q$ MeV in the pulse height histogram directly indicate the number of incident

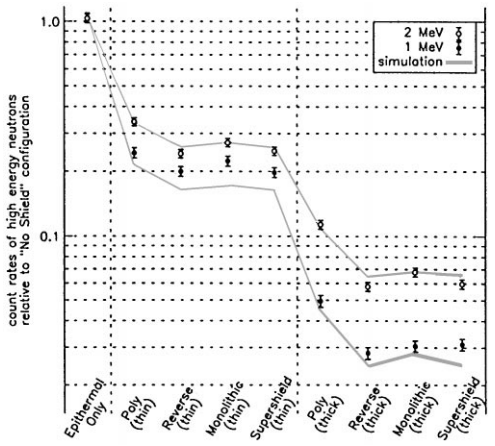

Fig. 6. Reduction of high energy neutrons: The data points are the integrated count rates within 100 keV of the high energy peak (1 + Q or 2 + Q MeV). The width of the line represents the statistical errors of the simulations. All the values are relative to the count rates in the "No Shield" configuration.

high-energy neutrons passing through the shields without interaction.

In the pulse height histogram of the ^{3}He counter, the high-energy peak at 1.764 MeV from the 1 MeV neutron source is located close to the pulse pile-up peak from epithermal neutrons, which is at two times of the Q-value (1.528 MeV). The relative strength of the pile-up changes, depending on the neutron beam intensity and shielding performance. To reduce the contributions from the pile-up and other effects, we make histograms from the events with pulse rise time slower than 1.4 μs, such as the shaded region in Fig. 3a. In Fig. 6 we plot the sum of the count rates within 100 keV of the high-energy peak of the histograms. The results are robust against different choices of the width around the peak.

All test shielding configurations reduced the incident neutron flux by a factor of five or more, depending on the thickness of the shields. There are only small variations among the "Reverse", "Monolithic", and "Supershield" configurations in Fig. 6. This is expected as these shields have approximately the same amount of hydrogen, which is responsible for removing (mostly by moderation) the high-energy neutrons. The small differences are due to other elements in the shields, the differences of the shield sizes, etc. The direct simulation results shown as shaded curves in Fig. 6 agree quite well with the experimental results. The slight discrepancy in the 1 MeV neutron results (for thin shields) is primarily due to imperfect subtraction of pulse pile-up and incomplete correction on the normalization offset in the ionization chamber (which monitored the beam intensity).

3.2.2. *Absorption of low-energy neutrons*: *thermal – 100 keV*

To find out how many neutrons are actually absorbed, we have to identify the intensity of low- and thermal-energy neutrons. The change in the number of detected low-energy neutrons indicates the change in the number of neutrons moderated but not absorbed in the test shield. The counts within 100 keV of the epithermal peak (764 keV) indicate the change of the neutron flux in the range from subthermal to $\sim$ 100 keV.

In this energy region there are unwanted counts from both epithermal and high-energy neutrons by recoil interactions and wall effects. Our simulations have shown that the data with the HENR in place represent the effects from epithermal neutrons, thus we determine the neutrons moderated down to low-energy but not absorbed by the test shields as follows:

(Neutrons moderated but not absorbed by the test shield) = (Counts without the HENR) − (Counts with the HENR).

The counts from recoil interactions can be easily estimated and taken out by the size of the recoil bump in the pulse height histogram (Fig. 3a). Other contamination remains negligible ($\lesssim 5\%$) by keeping the energy range of selection smaller than 100 keV.

Fig. 7 shows the count rates of events within 100 keV of the epithermal peak (pulse height channel 317–407 in Fig. 3a) after applying the above procedures. The differences of the various shield configurations in absorbing the moderated neutrons are evident. The "Supershield" configuration is superior to any other configuration in terms of suppressing low-energy neutrons.

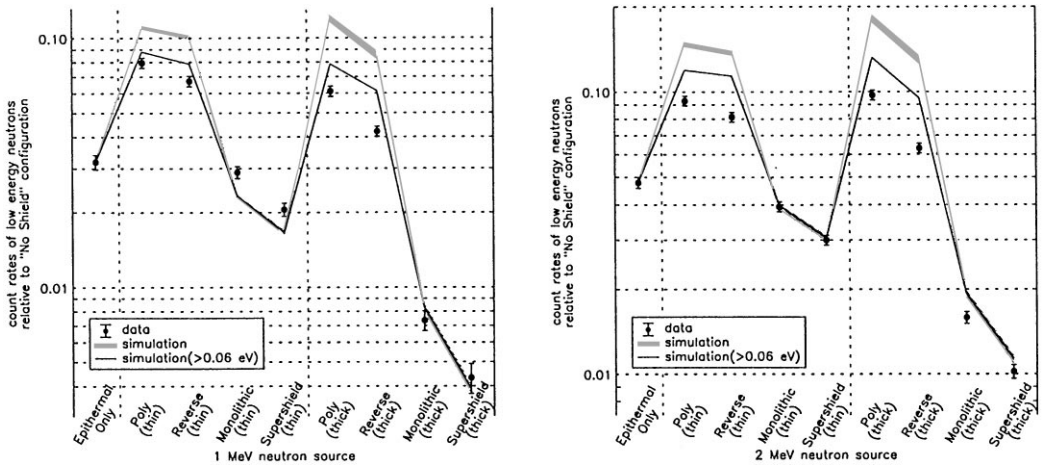

Fig. 7. Low and thermal neutron detection: The experimental results are relative to the "No Shield" configuration, and the normalization of simulations is adjusted to match the experimental value of the "Epithermal Only" configuration. The overestimation is simulations for the "Poly" and "Reverse" are probably caused by the (sub)thermal neutrons.

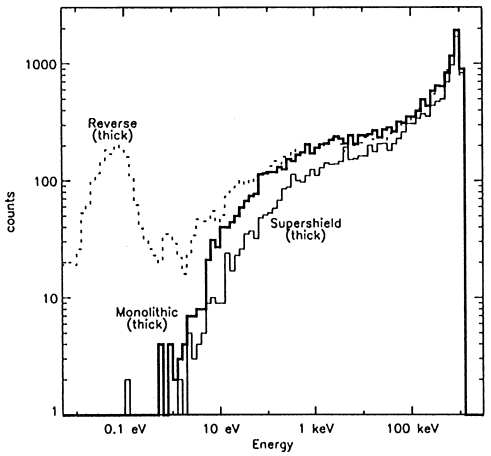

Fig. 8. The 1 MeV neutron flux entering the detectors: The "Monolithic" shield configuration gives results similar to those of the "Reverse" configuration at high energies and to the "Supershield" configuration at low energies.

The simulation results shown as shaded curves in Fig. 7 describe the data very well except for the "Poly" and "Reverse" configurations. Since counting the events around the thermal peak excludes the wall-effect events of the thermal and low-energy neutrons, we must determine the effect of the non-wall-effect events from the simulations.

According to the simulations, in both the "Poly" and "Reverse" configurations there are a substantial number of thermal neutrons entering the detector (see Fig. 8). The precise energy distribution of these thermal neutrons is important in estimating the exact number of non-wall-effect events since many subthermal neutrons have wall effects.[3] The energy distribution of these thermal neutrons depends on thermal motions of the atoms in the interacting material, which are determined by the temperature and the molecular structure of the material [15].

Even with the wall-effect-corrected efficiency calculations and the thermal-motion-corrected cross sections for neutron interactions of polyethylene, the simulations overestimate the neutrons in the "Poly" and "Reverse" configurations (Fig. 7). If one neglects the thermal neutrons, the simulations come into closer agreement with the experimental values (see solid lines in Fig. 7). Although the origin of the discrepancy in these two configurations is still not fully understood, we believe that it is due to

[3] Most subthermal neutrons interact with ^{3}He right after they enter the ^{3}He counter because of the high cross section for neutron absorption in ^{3}He. The interactions, therefore, occur very close to the detector wall and the majority of these interactions will lead to wall effects.

the impurity of the materials, incomplete subtraction of epithermal neutrons, and inaccurate correction for thermal motions of the molecules in the shield, which can affect thermal neutron distributions from the shields. In the cases of the "Supershield" and "Monolithic" configurations, the thermal neutrons are absorbed in the shields because of the high absorption cross section of boron, so that the simulation results do not depend on the above corrections.

We have compared the experimental and associated simulation results in high- and low-energy region and demonstrated the generally good agreement. Using COG simulations, we can now estimate the neutron spectra entering the ^{3}He counter over the entire energy range (Fig. 8).

The neutron spectrum of the "Monolithic" configuration lies between that of the "Reverse" and "Supershield" configurations. The spectrum in the "Monolithic" case is close to that of the "Reverse" at high energies while close to that of the "Supershield" configuration at low energies. As discussed previously, it is likely that the thermal neutrons in the "Reverse" configuration could be somewhat smaller than that the simulation predicts. The "Supershield" configuration is the optimal choice in suppressing neutron flux among these configurations.

4. Discussion

4.1. Relation to earlier simulations

The simulations performed using the COG package generally described the neutron transport process in this experiment quite well. The discrepancies noted between the experiments and the simulations for the "Reverse" and "Monolithic" shield configurations are due, at least in part, to lack of a detailed implementation of neutron scattering theory in the thermal energy region. COG is currently being coupled to the particle production code LAHET [16]. Using this coupled simulation code, we will be able to model complicated three-dimensional shields for a realistic experiment.

According to other Monte-Carlo simulations done in the past, monolithic shields were not expected to be effective in reducing certain types of detector background due to increased secondary particle production [6,7]. Although the superior performance of the supershield in neutron suppression is evident at any neutron energy, the performance difference measured between the supershield and monolithic shield in this particular experiment appears not so dramatic. The actual situation, however, is much more encouraging than might be expected given these earlier simulations.

The earlier studies on monolithic shields were conducted only for a particular case – ^{6}LiH-based shields for thick NaI detectors. It is difficult to generalize these results for other detectors and detector/shield combinations. For example, the neutron-induced background in a thin CdZnTe detector, especially with active shields on, is primarily due to high-energy neutrons, despite the high neutron absorption cross sections of ^{113}Cd at low energies [2]. The reason is that a neutron absorption interaction of ^{113}Cd produces three or four prompt γ-rays which can be easily vetoed by active shields. For a CdZnTe detector, therefore, suppressing just the high-energy neutrons can significantly reduce the neutron-induced background. The same condition does not apply in thick NaI detectors. In addition, the choice of absorbing materials, such as ^{10}B and ^{3}He, can increase by a factor of four the cross sections over those of ^{6}Li. Finally, the additional suppression offered by the supershield configuration, using ^{10}B- or ^{3}He-based shields, can achieve the same neutron absorption power with less shielding mass, which significantly reduces the secondary production.

The design of a supershield greatly influences its performance. Unlike a bi-atomic monolithic shield, there is an additional degree of freedom in designing supershields; the mass ratio of the absorber/moderator. In a bi-atomic monolithic shield, this ratio is fixed by the molecular structure of the material. In this experiment, the mass of the absorbing and moderating elements in the supershield was chosen to match roughly that in the monolithic shield for comparison. The energy of evaporative neutrons usually ranges from $\sim$ 500 keV to 10 MeV. For a given detector, therefore, once the most damaging neutron energy range and the total mass allowed for shielding material are determined, the

best mass ratio of absorber/moderator for the supershield can be chosen to optimally reduce the neutron-induced background.

4.2. Boron/hydrogen design issues

The main byproducts of a boron/hydrogen-based neutron shield are 480 keV and 2.2 MeV γ-rays released from the neutron absorption interactions of boron and hydrogen, respectively. Common hydrogen-bound materials, such as water, paraffin, and (boron-) polyethylene, contain a similar amount of hydrogen (~ 0.1 g/cm^3). Therefore, by using boron–polyethylene instead of just polyethylene in a supershield configuration, more neutrons and 2.2 MeV γ-rays can be suppressed without losing any moderation power, with the trade-off of producing more 480 keV γ-rays. For actual applications, one effective configuration of a boron- and hydrogen-based supershield is boron and boron–polyethylene, i.e. ^{10}B powder with ^{10}B-enriched boron–polyethylene (in realistic experiments, the enriched ^{10}B-based material is preferred to achieve better shielding performance with less material and less secondary particle production). For the experiments operating at high energies ($\gtrsim$600 keV), such a boron/hydrogen-based shield would be one of the optimal choices.

In fact, even for the experiments at low energies ($\lesssim$300 keV), a boron-based shield can be effectively utilized by using a proper active shield, since most 480 keV γ-rays Compton-scatter in a thin detector and they can be vetoed by the active shield. Boron-based shields, however, would be inappropriate for experiments designed to detect $\sim$480 keV γ-rays from astrophysical source, such as would be expected from red-shifted e^+e^- annihilation lines. In such experiments, neutron shields with ^{3}He-filled microspheres or other materials are preferred because ^{3}He does not have any γ-ray associated with the absorption interaction ^{3}He(n, p)T. The decay product of T, an 18.2 keV β particle, does not constitute an important background.

4.3. ^{3}He absorbers

^{3}He is an effective absorber for neutrons in a supershield configuration [1]. In the past ^{3}He was considered impractical to use for shielding in space applications, despite its high cross sections for neutron interactions, as it was not available in a safe, high-density state for effective shielding. Microspheres, developed for use in laser fusion experiments are perfectly formed small (~ 100 μm diameter) glass spheres that have been experimentally verified to hold gas up to several hundred atmospheres of pressure [17,18].

The technical difficulty in using ^{3}He-filled microsphere comes from the high permeability of ^{3}He. ^{3}He of ~ 100 bar differential pressure can leak out of regular glass in a few hours. Studies on gas permeation through glass, however, show that compounding the glass using Li or other elements can reduce permeability of ^{3}He by more than four orders of magnitude [19]. A properly compounded microsphere is expected to hold more than 1000 bar of ^{3}He for up to a few years at room temperature [18]. The neutron absorption power of 2000 atm ^{3}He-filled microspheres is equivalent to that of ~ 1 g/cm^3 ^{10}B-enriched boron powder (~ 4 mfp at 100 eV for 1 cm thickness).[4]

4.4. Applications for supershields

Various experiments can benefit from supershields. The CdZnTe detectors in the Energetic X-ray Imaging Survey Telescope (EXIST) are a typical example of a hard X-ray instrument where supershield technology can be applied [20]. EXIST is a coded-aperture, wide field of view survey mission, with a wide energy range ($\sim$ 5–600 keV). Several recent experiments on the background of CdZnTe detectors in space environments revealed higher background than expected [2,21,22]. In general, with active shields, the neutron-induced background is expected to be one of the dominant background sources for CdZnTe detectors at high energies ($\gtrsim$200 keV) [2]. As our experiment demonstrated, a properly designed supershield can readily suppress the high-energy neutrons, which are considered to be a dominant source of neutron-induced background in the EXIST CdZnTe detectors [2].

[4] Assuming 10/100 μm thickness/radius and $\sim$ 70% packing.

The natural choices of supershield materials for the wide energy range of EXIST are ^{3}He-filled microspheres and ^{6}LiH as an absorber/moderator. With these materials, neither the 0.48 nor 2.2 MeV γ-rays are generated as they would be in a boron or pure polyethylene configuration. The BGO shields covering $60 \times 60 \times 0.5$ cm^3 weigh about 72 kg in the baseline design of EXIST. If we baseline a factor of five or more reduction in the neutron-induced background only a 5 cm thick layer of ^{3}He/^{6}LiH would be required. This would only add 20–25 kg to total mission weight. Thus addressing the neutron background with the supershield concept will not impose any major burden on mass constraints (nor will the small amount of additional material produce major increases in the rates of secondary particles).

The total size of active shields is usually limited by mass constraints on the payload and the secondary particle production (especially neutrons) in the shields themselves. Since supershields alleviate the problem of the neutron production in the active shields, there is no stringent limit in the total size of active shields for experiments without severe mass constraints. In a space station version of EXIST (EXIST-ISS) employing supershields, for example, active shield volume can be added to improve background rejection efficiency without regard to the increased secondary production [23].

5. Conclusion and future work

This experiment showed that supershields enable better neutron-induced background rejection than other test shields. We have demonstrated that a ~ 5 cm thick supershield reduces the incident high-energy neutron flux by more than a factor of five. The supershield also showed $\sim 50\%$ higher suppression in low-energy neutrons than a monolithic shield (which combines the moderator and absorber in one layer).

We also explored the possible choices of materials and configurations for supershields in realistic experiments. We discussed the potential future uses of supershields in hard X-ray experiments such as EXIST.

Generally the boron-based materials we worked with in this series of experiments should be avoided in instruments that are focused on detecting ~ 480 keV γ-ray. Future work will be concentrated on materials, such as ^{3}He-filled microspheres, that are optimized to avoid contamination in this energy range. Future experiments will include a prototype γ-ray detector and appropriate active shields, along with fully modeled three-dimensional supershields. Future work will also include the simulations of realistic space experiments using Monte-Carlo simulation code that couples particle production and neutron transport.

Acknowledgements

We wish to thank Professor David J. Brenner of Columbia University for permitting us to use RARAF and Stephen A. Marino for technical assistance. We also thank Irwin Rochwarger for technical advices on electronics. This work was supported by the NASA Innovative Research Program under grant NAGW-4818.

References

[1] C.J. Hailey, F.A. Harrison, Nucl. Instr. and Meth. A 365 (1995) 518.
[2] F. Harrison et al., Nucl. Instr. and Meth. (2000), in press.
[3] C. Winkler, O. Pace, S. Volonté, ESA J. (1993) 207.
[4] P. Jean et al., Proceedings of Second INTEGRAL Workshop, 1997, p. 635.
[5] G. Vedrenne et al., Multifrequency behaviour of high energy sources, Mem S.A.It., Vol. 69, No. 4, 1998.
[6] C.S. Dyer et al., IEEE Trans. Nucl. Sci. NS-34 (6) (1987) 1530.
[7] C.S. Dyer et al., IEEE Trans. Nucl. Sci. NS-35 (6) (1988) 1407.
[8] J. Hong, C.J. Hailey, Proceedings of SPIE: Gamma-Ray and Cosmic-Ray Detectors, Techniques, and Missions, Vol. 2806, 1996, p. 449.
[9] H. Liskien, A. Paulen, Nucl. Data Tables 11 (1973) 569.
[10] G.F. Knoll, Radiation Detection and Measurement, Wiley, New York, 1979.
[11] A. Sayres, M. Coppola, Rev. Sci. Instr. 35 (1964) 431.
[12] S. Izumi, Y. Murata, Nucl. Instr. and Meth. 94 (1971) 141.
[13] S. Shalev, Z. Fishelson, J.M. Cuttler, Nucl. Instr. and Meth. 71 (1969) 292.
[14] T.P. Wilcox Jr., E.M. Lent, Lawrence Livermore National Laboratory Report, M-221-1, 4, 1989.

[15] J. Keinert, Temperature dependence of thermal neutron scattering cross sections for hydrogen bound in moderators, Karlsruhe, Fachinformationszentrum Energie, Physik, Mathematik GmbH, Germany, 1982.
[16] R.E. Prael, H. Lichtenstein, User Guide to LCS: The LAHET Code System, Low Alamos National Laboratory Report, LA-UR-89-3014, 1989.
[17] S.M. Aceves, G.D. Berry, G.D. Rambach, Int. J. Hydrogen Energy 23 (1998) 583.
[18] V.M. Dorogotovtsev, Proceedings of the Symposium MRS: Hollow and Solid Spheres and Microspheres: Science and Technology Associated with their Fabrication and Application, Vol. 372, 1995, p. 131.
[19] R.H. Doremus, Treatise on Material Science and Technology, Vol. 17, Academic Press, INC. (London) LTD., USA, 1979.
[20] J.E. Grindlay, Astron. Nach. 319 (1998) 133.
[21] A.M. Parsons et al., Proceedings of SPIE: Gamma-Ray and Cosmic-Ray Detectors, Techniques, and Missions, Vol. 2806, October 1996, pp. 432–441.
[22] P.F. Bloser, Proceedings of SPIE: EUV, X-Ray, and Gamma-Ray Instrumentation for Astronomy IX, Vol. 3445, November 1998, pp. 186–196.
[23] J.E. Grindlay et al., Proceedings of the Fifth Compton Symposium, AIP Conf. Proc., Vol. 510, 1999, p. 784.